

# Solid-state polymer electrolytes with in-built fast interfacial transport for secondary lithium batteries

Qing Zhao<sup>1</sup>, Xiaotun Liu<sup>1</sup>, Sanjuna Stalin<sup>1</sup>, Kasim Khan<sup>1</sup> and Lynden A. Archer<sup>1,2\*</sup>

**Solid-state electrolytes with high room-temperature ionic conductivity and fast interfacial charge transport are a requirement for practical solid-state batteries. Here, we report that cationic aluminium species initiate ring-opening polymerization of molecular ethers inside an electrochemical cell to produce solid-state polymer electrolytes (SPEs), which retain conformal interfacial contact with all cell components. SPEs exhibit high ionic conductivity at room temperature ( $>1\text{ mS cm}^{-1}$ ), low interfacial resistances, uniform lithium deposition and high Li plating/stripping efficiencies ( $>98\%$  after 300 charge-discharge cycles). Applications of SPEs in Li-S, Li-LiFePO<sub>4</sub> and Li-LiNi<sub>0.6</sub>Mn<sub>0.2</sub>Co<sub>0.2</sub>O<sub>2</sub> batteries further demonstrate that high Coulombic efficiency ( $>99\%$ ) and long life ( $>700$  cycles) can be achieved with an in situ SPE design. Our study therefore provides a promising direction for creating solid electrolytes that meet both the bulk and interfacial conductivity requirements for practical solid polymer batteries.**

In pursuit of high-energy-density electrical energy storage/conversion devices, rechargeable batteries that employ metals, including lithium and sodium, as anodes have gained attention recently<sup>1–3</sup>. However, it is known that, even at current densities below the diffusion limiting current, where most batteries are operated, poor chemical stability of liquid electrolytes in contact with the metal anode limits both the performance and safety of such cells<sup>4–8</sup>. Premature battery failure may occur by a direct parasitic process, wherein the electrolyte continuously reacts with the electrode to deplete the electrolyte, thicken the electrode/electrolyte interphases, and produce run-away cell resistances<sup>9</sup>. Failure may also result from indirect processes produced by dendrite-induced internal short circuits<sup>10</sup>. Approaches including the design of sacrificial additives<sup>11</sup>, assembly of artificial solid electrolyte interphase (SEI) layers<sup>12</sup>, and structured electrolytes (highly concentrated solvent-in-salt liquids<sup>13–15</sup>, nanoporous solids<sup>16</sup> and solid-state electrolytes<sup>17</sup>) have been applied to address these challenges with increasingly high levels of success. Solid-state electrolytes (SSE) are considered particularly promising because of their inherent safety characteristics and potential to prevent dendritic deposition of the metal<sup>18</sup>.

Two principal types of SSEs have been studied to date: SSEs based on ion-conducting inorganic solids<sup>19,20</sup> and SSEs based on organic polymers (so-called solid-state polymer electrolytes (SPEs))<sup>21–23</sup>. SPEs are considered attractive from a range of perspectives, including their superior mechanical toughness, lower cost, lightweight characteristics and compatibility with large-scale roll-to-roll manufacturing processes. In general, a successful SPE is required to have at least two characteristics. First, it should enable high bulk ionic conductivity and fast interfacial transport of Li ions at both the anode and cathode of a battery. Second, it should remain mechanically stable and chemically inert during extended battery cycling. The most studied SPEs based on lithium bis(trifluoromethylsulfonyl)imide (LiTFSI) in poly(ethylene oxide) do not meet either of these requirements at room temperature.

Various strategies have been reported in the literature to improve the electrochemical and mechanical properties of SPEs<sup>24–27</sup>. The addition of inorganic fillers, either by physical mixing or by chemically tethering polymer chains to inorganic nanostructures, has been used to create so-called hybrid SPEs with increased room temperature ionic conductivity<sup>28</sup>. Cross-linked SPEs created using ultraviolet/thermal polymerization provide a straightforward approach for the scalable synthesis of SPEs with balanced mechanical and ion-transport features<sup>29–31</sup>. SPEs containing two or more salts and a plastic crystal plasticizer have been reported to exhibit both high ionic conductivity and high voltage stability<sup>32</sup>. Near-single Li-ion-conducting SPEs have been created by appending polyanions<sup>33,34</sup> and ionic liquids<sup>35,36</sup> to a polymer backbone.

The hypothesis that motivates the present study is that forming SPEs in situ by polymerization of a liquid precursor would address the low ionic conductivity and high interface resistance of SPEs. Specifically, we take advantage of the beneficial properties of liquids, including low viscosity and easy handling, and the ability to wet and thereby create good interfacial contact with interfaces at essentially all length scales, to create electrochemical cells with well-connected pathways for ionic transport that enable full access to the active materials (Fig. 1a). Subsequent polymerization of the liquid electrolyte in the fully formed battery transforms the electrolyte from a liquid-state material to a solid-state material. Beyond the obvious benefits already discussed, the approach also produces SPEs of high purity (that is, comparable to those achieved with current liquid electrolytes); provides a facile method for repairing bulk and interfacial defects in a SPE or ceramic SSE produced during electrolyte manufacture or battery assembly; and the same procedures in current use for electrolyte handling and filling can be employed. We evaluate our hypothesis by performing ring-opening polymerization of 1,3-dioxolane (DOL) inside an electrochemical cell to produce the solid-state analogue of an electrolyte based on this material. As a common low-molar-mass ether solvent with low dielectric constant ( $\epsilon \sim 7$ )<sup>37</sup>, ring-opening polymerization of DOL

<sup>1</sup>Robert Frederick Smith School of Chemical and Biomolecular Engineering, Cornell University, Ithaca, NY, USA. <sup>2</sup>Department of Materials Science and Engineering, Cornell University, Ithaca, NY, USA. \*e-mail: [laa25@cornell.edu](mailto:laa25@cornell.edu)

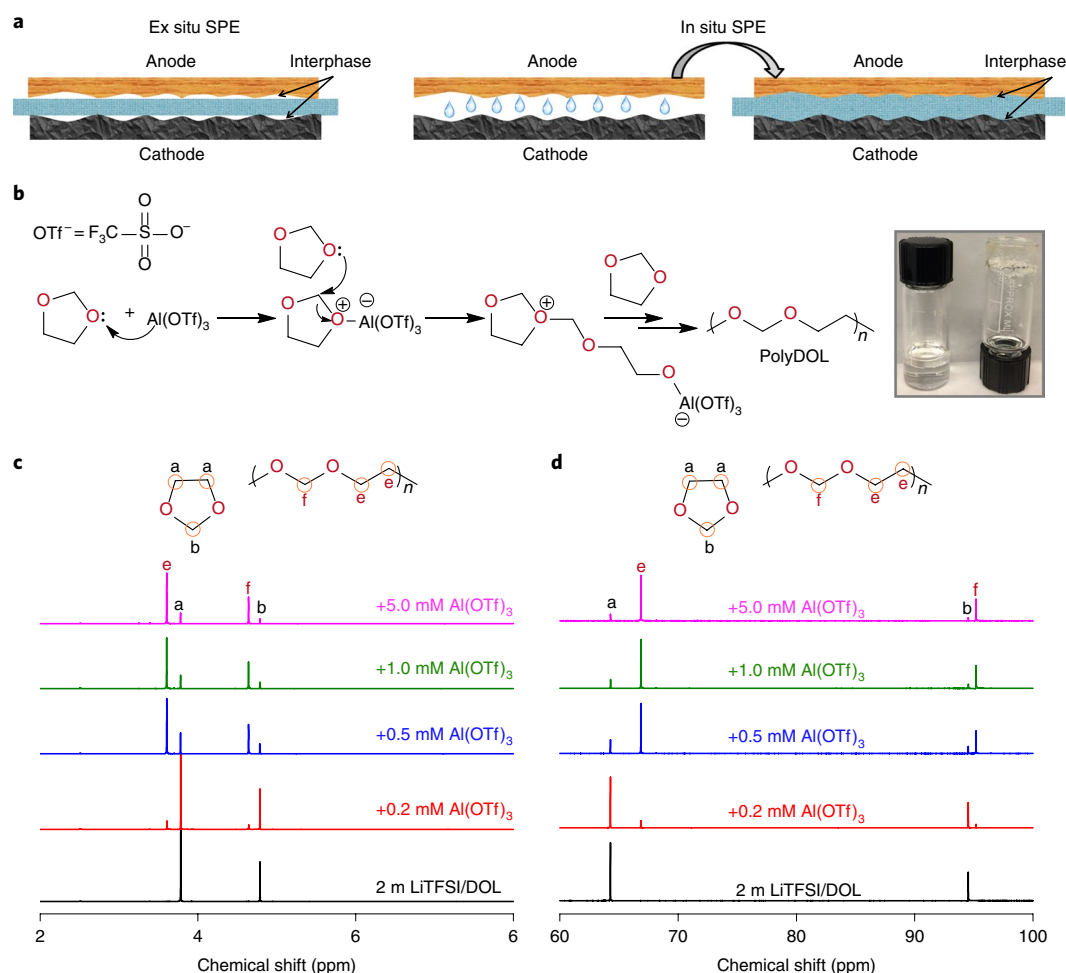


**Fig. 1 | Preparation of SPEs. a**, Schematic illustrating ex situ and in situ synthesis of SPEs. Ex situ synthesis results in higher interphase resistance due to poor contact with other cell components. The liquid precursors of SPEs formed by in situ synthesis are able to wet, and create good interfacial contact with, cell components; these contacts are preserved when the electrolyte is polymerized. **b**, Reaction mechanism illustrating how  $\text{Al(OTf)}_3$  initiates polymerization of DOL. Inset: digital photograph depicting the liquid DOL electrolyte (2 m LiTFSI/DOL, left) and solid-state poly-DOL electrolyte formed spontaneously in an electrolyte containing 0.5 mM  $\text{Al(OTf)}_3$  salt (right). **c, d**, Hydrogen (**c**) and carbon (**d**) NMR spectra of liquid DOL and the poly-DOL SPE formed at different  $\text{Al(OTf)}_3$  concentrations.

has been studied for over 50 years. In 1964, Okada et al.<sup>38</sup> reported that, in the presence of water, some organo-aluminium compounds, such as diethyl aluminium chloride and ethyl aluminium dichloride, initiate polymerization of DOL. Here, we are interested in electrolyte salts that exhibit similar activity, but without adding water. The results reported here show that aluminium triflate ( $\text{Al}(\text{CF}_3\text{SO}_3)_3$ ) and  $\text{Al(OTf)}_3$  salts are efficient initiators for the polymerization of DOL and can be used to transform a DOL-based liquid electrolyte to a SPE at concentrations as low as 0.5 mM. We show that SPEs created in this manner overcome the most serious limitations of conventional SPEs.

### Structure, composition and kinetics of prepared SPEs

Figure 1 summarizes the essential chemical process whereby  $\text{Al(OTf)}_3$  initiates polymerization of DOL and transforms a liquid DOL-based electrolyte to an SPE. As illustrated in Fig. 1b, the reaction is initiated by a cationic aluminium species in solution. The aluminium-based cation first attaches to the oxygen atom and initiates the ring-open polymerization. The inset digital picture in Fig. 1b shows that, on addition of as little as 0.5 mM  $\text{Al(OTf)}_3$ , the originally liquid LiTFSI-DOL electrolyte is transformed to a transparent, solid product. NMR analysis (Fig. 1c,d) confirms that

the material is poly-DOL. Specifically, after the polymerization reaction, new hydrogen and carbon peaks are observed, which are in accordance with the structure of poly-DOL. In addition, the ratio of unpolymerized DOL and poly-DOL can be estimated by integrating the peak area of the  $^1\text{H}$  NMR spectra. The results summarized in Supplementary Table 1 show that the unpolymerized DOL fraction accounts, respectively, for 86, 19, 14 and 10% in the electrolytes formed at 0.2, 0.5, 1.0 and 5.0 mM  $\text{Al(OTf)}_3$  initiator. These changes in composition occur in tandem with structural evolution, as reported by Fourier-transform infrared spectroscopy (FTIR) (Supplementary Fig. 1) and Raman spectroscopy analysis (Supplementary Fig. 2). While electrolyte with 0.2 mM  $\text{Al(OTf)}_3$  manifests characteristic vibrations of the liquid DOL precursor, increasing the  $\text{Al(OTf)}_3$  content to 0.5 mM produces a virtual disappearance of the ring vibration, large shifts in the C–O–C vibration and emergence of vibration modes associated with long-chain species.

The weight-averaged molecular weights ( $M_w$ ) of the poly-DOL were analysed by gel permeation chromatography. The results reported in Supplementary Table 1 show that the molecular weight and polydispersity index ( $M_w/M_n$ ) ( $M_n$  is the number-average molecular weight) of the poly-DOL generally decrease approximately

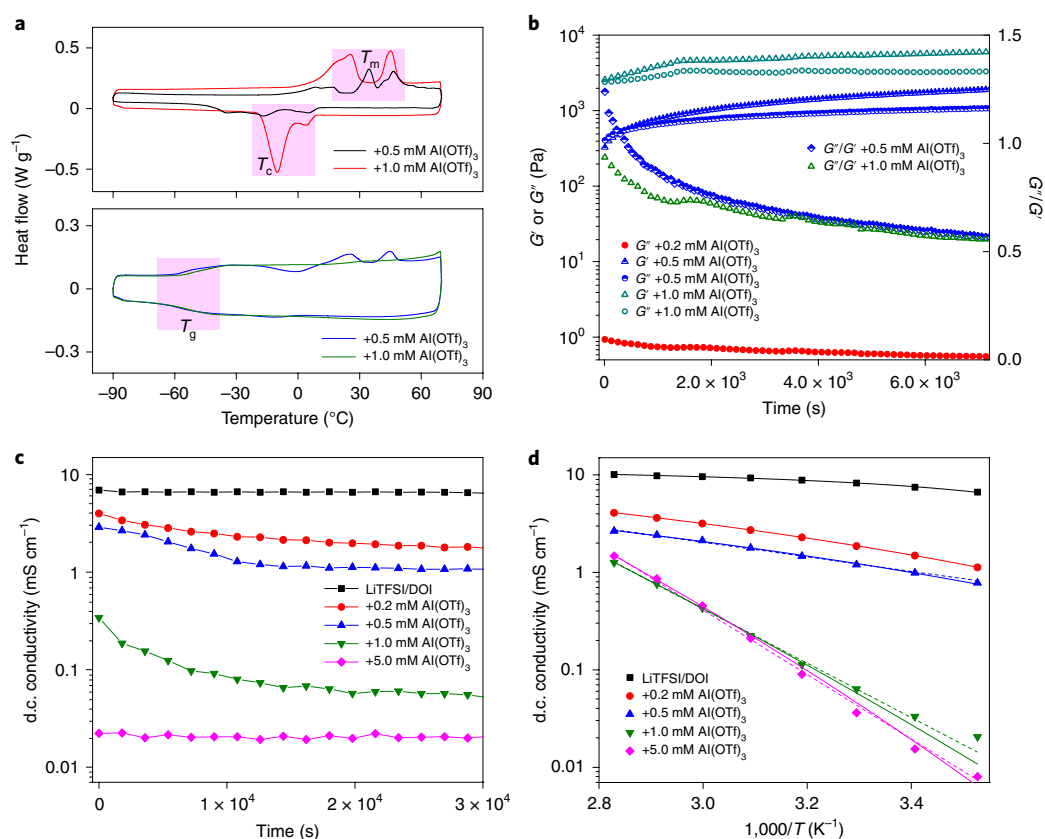


**Fig. 2 | Kinetics and electrochemical characteristics of SPEs with different concentrations of  $\text{Al}(\text{OTf})_3$ .** **a**, DSC analysis of poly-DOL (without LiTFSI, top) and the poly-DOL electrolyte (with LiTFSI, bottom). The shaded areas show the melting peak ( $T_m$ ), recrystallization peak ( $T_c$ ) and glass transition peak ( $T_g$ ), respectively. **b**, Dynamic storage ( $G'$ ) and loss ( $G''$ ) moduli (Pa) and loss tangent ( $\tan\delta = G''/G'$ ) versus time for the poly-DOL electrolyte. **c**, d.c. conductivity versus polymerization time for the SPE. **d**, d.c. conductivity of the poly-DOL electrolyte versus temperature. The solid and dashed lines through the data are fits using the Vogel-Fulcher-Tammann and Arrhenius transport models, respectively.

as the inverse of the  $\text{Al}(\text{OTf})_3$  concentration, which is precisely the relationship one would expect if  $\text{Al}(\text{OTf})_3$  functioned as an initiator for the ring-opening polymerization reaction. Specifically, the higher concentration of  $\text{Al}(\text{OTf})_3$  increases the initiation rate, causing more polymer chain formation, which would lower the overall polymer molecular weight—precisely what is observed. Additionally, because the DOL functions as both reactant and solvent, the polymer chain would become smaller—for reactant transport reasons, with increasing  $\text{Al}(\text{OTf})_3$  content. Comparison of the poly-DOL molecular weights formed in our synthesis with the entanglement molecular weight ( $M_e$ ) of  $\sim 1,200$  Da estimated from the packing model<sup>39</sup> implies that at the lower  $\text{Al}(\text{OTf})_3$  concentrations, the polymer exists minimally as a physical network of interconnected/entangled chains.

Differential scanning calorimetry (DSC) was applied to study thermal transitions in the poly-DOL from heat flow measurements. The results reported in Fig. 2a and Supplementary Fig. 3 show that, whereas the salt-free poly-DOL is crystalline, the electrolyte (poly-DOL + 2 m LiTFSI, where 1 m stands for 1 M salt dissolved in 1 l solvent) is essentially amorphous. Typical peaks associated with the melting ( $T_m$ ) and recrystallization ( $T_c$ ) of the salt-free poly-DOL material are observed. However, only a glass transition peak ( $T_g$ ) is observed for the poly-DOL electrolytes. We believe that the absence of crystallization in the in situ-formed poly-DOL electrolytes is a key determinant of their high bulk and interfacial ionic conductivities. Thermogravimetric analysis (TGA) demonstrates that the thermal stability is largely improved after transferring liquid DOL electrolyte to poly-SPE (Supplementary Fig. 4).

The kinetics of the polymerization process were studied next by means of time-dependent changes in the elastic and ion transport properties of the electrolyte. The results reported in Fig. 2b show that both the elastic/storage modulus ( $G'$ ) and viscous/loss modulus ( $G''$ ) deduced from dynamic shear rheology measurements of the reaction mixture increase over time, reflecting the rising contribution of growing polymer chains to the rheological characteristics of the electrolytes. For electrolytes containing 0.5 mM  $\text{Al}(\text{OTf})_3$  catalyst, at early times ( $t < 600$  s), the loss modulus is dominant (that is,  $G'' > G'$ ), indicating that the electrolytes are liquid-like. As the reaction proceeds,  $G'$  is observed to become more dominant, indicative of a transition to solid-like, elastic behaviour as the growing polymer chains begin to form physical entanglements with their neighbours. At long times, both moduli approach a constant, limiting value, and their ratio ( $\tan\delta = G''/G'$ ), termed the loss tangent, approaches a constant value below unity. This behaviour is consistent with the onset of solid-like behaviour of elastic materials in which each material element is localized in a cage with 'localization length'<sup>40</sup>:  $\xi = (k_B T / G_0)^{1/3}$  ( $\xi \cong 12.7$  nm). At double (1 mM) the  $\text{Al}(\text{OTf})_3$  concentration, both moduli are obviously higher and the rate at which they approach steady state increases noticeably. The  $\tan\delta$  plot shows that, at the higher  $\text{Al}(\text{OTf})_3$  concentration, the electrolytes are more solid-like, and the calculated localization length,  $\xi \sim 8.7$  nm, bears this out. In contrast, an elastic contribution cannot be observed at an  $\text{Al}(\text{OTf})_3$  concentration of 0.2 mM due to the low polymer fraction, despite the higher  $M_w$  of  $\sim 49$  K revealed by gel permeation chromatography (GPC) analysis. The dynamic mechanical properties of the prepared SPE were also studied by small-amplitude

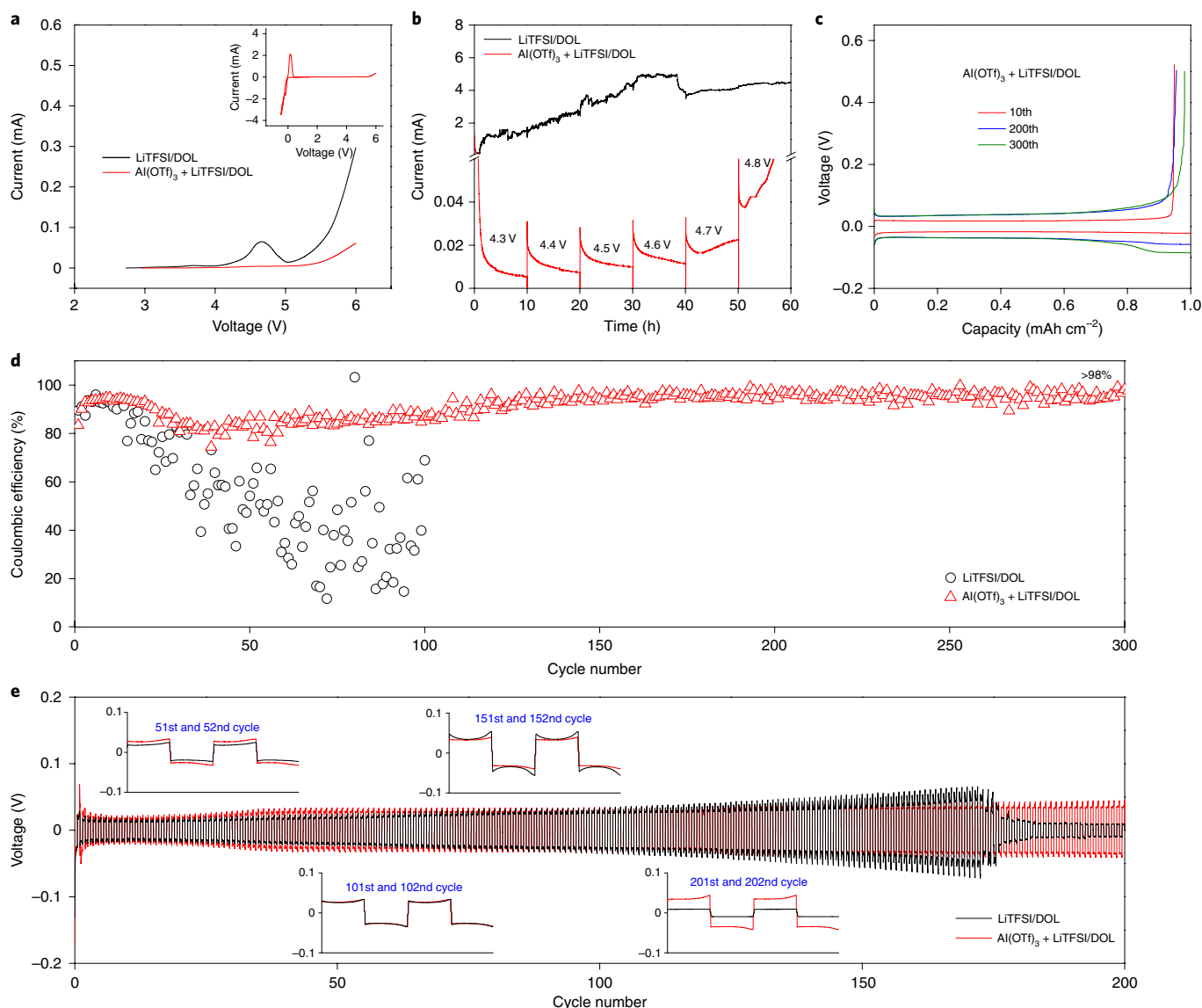


**Fig. 3 | Electrochemical stability of the poly-DOL electrolyte.** **a**, Linear sweep voltammetry of the liquid DOL (2 m LiTFSI/DOL) electrolyte and poly-DOL SPEs (0.5 mM  $\text{Al}(\text{OTf})_3$  + 2 m LiTFSI/DOL) at a sweep rate of  $1 \text{ mV s}^{-1}$ . Inset: current-voltage curves for Li plating and stripping in poly-DOL SPEs at a sweep rate of  $1 \text{ mV s}^{-1}$ . **b**, Electrochemical floating analysis of the liquid DOL electrolyte and poly-DOL SPEs using NMC cathodes. **c**, Li stripping and plating profiles as a function of cycle number, obtained using poly-DOL SPEs. **d**, Corresponding Coulombic efficiencies as a function of cycle number for the liquid DOL electrolyte and poly-DOL SPE. The current density is  $1 \text{ mA cm}^{-2}$  and the plating Li capacity is  $1 \text{ mAh cm}^{-2}$  per cycle. **e**, Long-term cycling of symmetrical Li cells using the liquid DOL electrolyte and poly-DOL SPE. The current density is  $1 \text{ mA cm}^{-2}$ , and  $1 \text{ mAh cm}^{-2}$  Li is plated and stripped per cycle. Insets: enlarged profiles at the two consecutive cycle numbers noted.

oscillatory shear measurements (Supplementary Fig. 5) and tensile analysis (Supplementary Fig. 6), which also provides fundamental support for their classification as SPEs.

The change of d.c. conductivity versus time (Fig. 2c) provides an additional approach for following the polymerization reaction and evaluating the transport properties of SPEs as a function of  $\text{Al}(\text{OTf})_3$  concentration. The results show that the ionic conductivity of poly-DOL electrolytes with 0.5 mM  $\text{Al}(\text{OTf})_3$  drops during the first 3 h after initiating the ring-opening reaction, and approaches a constant value of approximately  $1 \text{ mS cm}^{-1}$  over longer durations. These long-time ionic conductivity values are higher than is typical for SPEs at room temperature. They may imply that even at long times and steady state, the polymerization reaction cannot reach completion and a small amount of unpolymerized or incompletely

polymerized DOL remains bound in the entangled polymer. This mobile fluid fraction would be expected to facilitate both bulk and interfacial ion transport. NMR analysis of SPEs confirms this view and, in fact, shows that depending on the concentration of  $\text{Al}(\text{OTf})_3$  in the precursor liquid electrolyte, the extent of the polymerization reaction can be manipulated to produce varying amounts of residual unpolymerized DOL in the poly-DOL host material. Increasing the concentration of  $\text{Al}(\text{OTf})_3$  above approximately 1 mM produces a sharply lower ionic conductivity (below  $0.1 \text{ mS}$  at steady state, which is thought to arise from the greater solidification and smaller localization length of poly-DOL SPEs.

Fig. 2d reports on the temperature-dependent ionic conductivity of in situ-formed SPEs. The solid lines through the data were obtained by fitting the measured values using the Vogel–Fulcher–

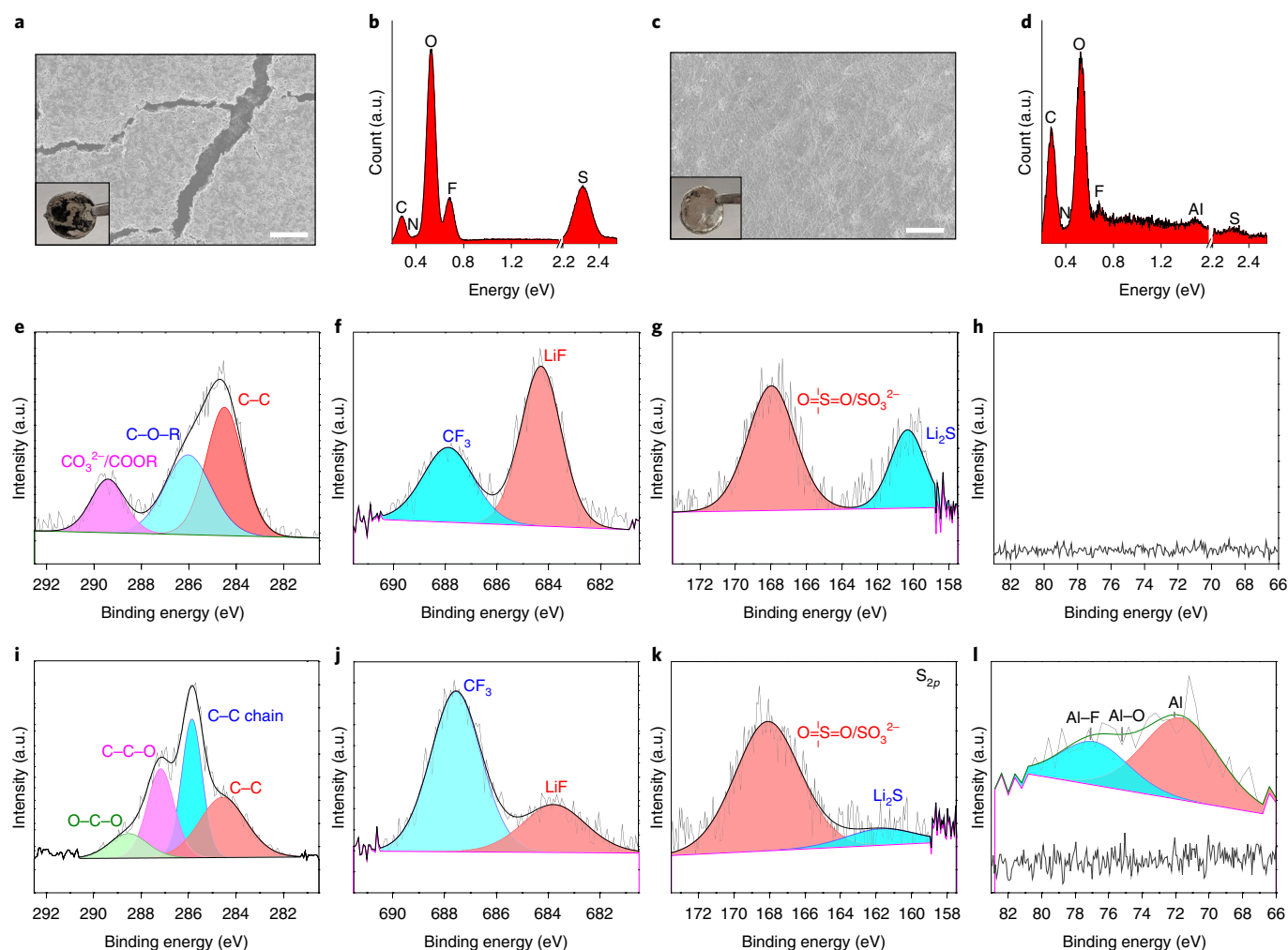


**Fig. 4 | Characterization of SEI formed on Li cycled in liquid DOL and SPE electrolytes.** **a–d**, SEM images (**a** and **c**) and EDX analyses (**b** and **d**) of cycled Li electrodes collected from symmetrical Li cells utilizing liquid electrolytes (**a** and **b**) or poly-DOL SPEs (**c** and **d**) after the 50th cycle. Insets in **a** and **c** are digital pictures. Scale bars, 20  $\mu\text{m}$ . **e–l**, Corresponding XPS analyses for C 1s (**e** and **i**), F 1s (**f** and **j**), S 2p (**g** and **k**) and Al 2p (**h** and **l**) performed on cycled Li electrodes for cells that utilized liquid electrolytes (**e–h**) and poly-DOL SPEs (**i–l**). The Al 2p spectra of the Li electrode using SPE before cycling are also listed for comparison. The wide blue peak in **l** is assigned to ionic Al<sup>3+</sup> associated with Al-F or Al-O, and the red peak is assigned to metallic Al.

Tammann model, while the dashed lines were obtained using the Arrhenius model. At higher Al(OTf)<sub>3</sub> concentrations, the measured conductivity is seen to be well described by either model, which is expected because the ionic conductivity is measured at temperatures far beyond the glass transition temperature. Closer inspection of the results nonetheless reveals that the Arrhenius expression provides a slightly better account of the low temperature conductivity, particularly at high Al(OTf)<sub>3</sub> concentrations (1 and 5 mM). Our observations suggest that the ion motions are decoupled from long-range motions of the polymer chains and may progress by an ion rafting process, wherein the unpolymerized component in the materials is the ion carrier at all Al(OTf)<sub>3</sub> concentrations. More detailed studies of ion transport over a wider range of temperatures are underway to evaluate this hypothesis.

### Electrochemical properties of in situ-formed SPEs

The DOL-LiTFSI electrolyte precursor used to create our SPEs is not commonly used in Li batteries that employ intercalating cathodes because of its relatively poor oxidative stability at potentials above 4 V (versus Li<sup>+</sup>/Li). Linear sweep voltammetry measurements were used to determine the effect of polymerizing a liquid DOL electrolyte on the electrochemical stability window of the material.

The results reported in Fig. 3a clearly show that polymerization dramatically increases the oxidative stability to over 5 V. These same measurements show that for the liquid DOL-LiTFSI electrolyte, oxidation already occurs at around 4.2 V (Fig. 3a and Supplementary Fig. 7). In a wider-range scan from –0.2 to 6 V, the results show that polymerization does not compromise the excellent Li stripping/plating profiles (inset in Fig. 3a).

The electrochemical floating experiment provides a more stringent test of the oxidative stability of in situ-formed poly-DOL SPEs<sup>41</sup>. The leakage current measured during the experiment provides a straightforward means of assessing the oxidative stability of an electrolyte. The results reported in Fig. 3b show that at voltages below 4.7 V, the leakage current measured in SPEs is small (< 20  $\mu\text{A}$ ). In contrast, similar experiments using the liquid LiTFSI/DOL electrolyte reveal leakage currents exceeding 1 mA at voltages as low as 4.3 V. A key hypothesis of our work is that in situ formation of SPEs provides an opportunity to overcome the traditionally high interfacial resistances characteristic of SSEs (Supplementary Fig. 8). A second hypothesis is that polymerization of a liquid electrolyte will reduce its reactivity towards a metallic Li anode, resulting in higher Coulombic efficiency and lithium metal batteries with longer-term stability.



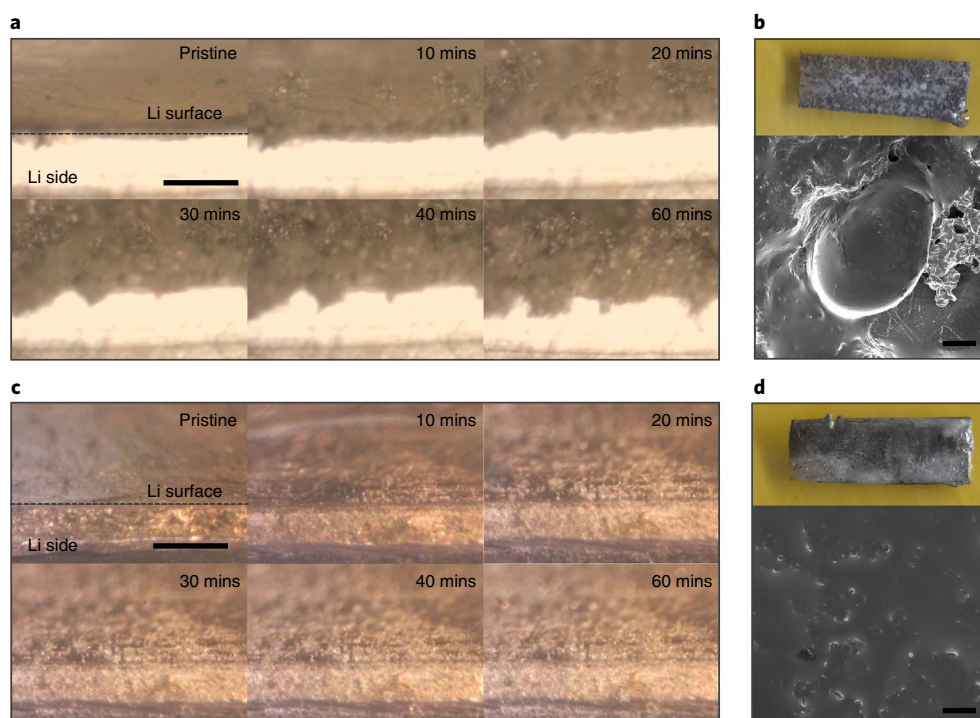


**Fig. 5 | Li electrodeposit morphology in the liquid electrolyte and poly-DOL SPEs. a–d,** Morphological evolution of electrodeposited Li characterized by real-time optical microscopy (**a** and **c**) and corresponding optical (top) and SEM images (bottom) of the Li metal electrode after Li plating (**b** and **d**) in a liquid electrolyte (**a** and **b**) and a poly-DOL SPE (**c** and **d**). The current density was  $2 \text{ mA cm}^{-2}$  and the test lasted for 60 min. Scale bars:  $500 \mu\text{m}$  in **a** and **c** and  $50 \mu\text{m}$  in **b** and **d**.

Figure 3c and Supplementary Fig. 9 compare the results from galvanostatic polarization experiments for the liquid DOL electrolyte and in situ SPEs. SPEs with  $0.5 \text{ mM Al}^{3+}$  were selected for in-depth study for two principal reasons. First, they show typical characteristics of SPEs, including existence as a free-standing film and manifesting viscoelastic solid-like properties in shear and tensile testing experiments. Second, in comparison with SPEs formed at higher  $\text{Al}^{3+}$  contents, SPEs with  $0.5 \text{ mM Al}^{3+}$  exhibit the highest combination of mechanical modulus and room temperature ionic conductivity. Both measurements were performed in asymmetric  $\text{Li}||\text{Cu}$  cells at a current density of  $1 \text{ mA cm}^{-2}$ . Although the liquid electrolyte shows small polarization between Li stripping and plating, the Coulombic efficiency fades quite quickly (Fig. 3d and Supplementary Fig. 10). We attribute this behaviour to the continuous reduction of DOL by the freshly deposited Li metal in each cycle, which continuously consumes the electrolyte, thickens the SEI on Li, and limits access to the electrodeposited Li metal. In comparison, Li–Cu batteries with SPEs show consistent and high Coulombic efficiency ( $>98\%$ ), even after 300 Li strip–plate cycles.

The reversibility of Li plating and stripping processes in in situ-formed poly-DOL SPEs and their unpolymerized liquid analogues was investigated in symmetric Li cells. As shown in Fig. 3e, for the initial tens of cycles, lower polarization is observed in the liquid electrolytes, presumably because of their higher ionic conductivity. However, after 100 cycles, an obvious but gradual increase in the peak-to-peak voltage is evident for measurements performed in liquid electrolytes. This increase is indicative of the greater difficulty of nucleating Li during the plating segment of the cycle and stripping Li during the reversing segment of the cycle, and the overall deposition of Li. It is normally associated with the formation of a thick SEI at the electrode and the accumulation of electronically disconnected/dead Li fibrils at the interface<sup>42</sup>. The process typically

ends with a sudden, permanent drop in peak-to-peak voltage and a noticeable squaring of the edges of the voltage profile (see inset in Fig. 3e for the 201st and 202nd cycle), which is thought to arise from the formation of one or more internal short circuits as the Li deposits grow uncontrollably at local regions of the electrode to bridge the inter-electrode space. In comparison, SPE cells continue to operate stably beyond 200 cycles. In addition, the structure of poly-DOL SPEs is unchanged from the beginning to the end of the cycling (see FTIR (Supplementary Fig. 11) and NMR spectra (Supplementary Fig. 12)).

### SEI and Li electrodeposition

The components and chemical states of SEI formed on an Li metal anode using poly-DOL electrolytes were also studied. The Li harvested from cells in which liquid DOL was the electrolyte manifested a distinctive black colouration after cycling, and obvious cracks are shown in Fig. 4a. In contrast, the surfaces of Li harvested from cells based on the poly-DOL electrolyte exhibited almost no change in colour, and compact, flat topography after 50 cycles (Fig. 4c). According to energy-dispersive X-ray spectroscopy (EDX) analysis, the major elements on the cycled Li anode in the liquid DOL electrolyte are carbon, oxygen, fluorine and sulfur (Fig. 4b). In the case of poly-DOL SPEs, we not only found these four elements, but also discovered a small amount of aluminium (Fig. 4d). In general, the counts/intensity for liquid DOL are much higher than for poly-DOL SPEs, indicating substantial thin SEI formed on the surface of the metal Li using poly-DOL SPEs. Further X-ray photoelectron spectroscopy (XPS) spectra were used to characterize the chemical state of the SEI in both systems (Fig. 4e–i). The C1s spectra show considerably higher binding energy peaks for the liquid DOL electrolyte, which should belong to the decomposition of DOL and formation of  $\text{CO}_3^{2-}$  and COOR components (Fig. 4e)<sup>43,44</sup>.

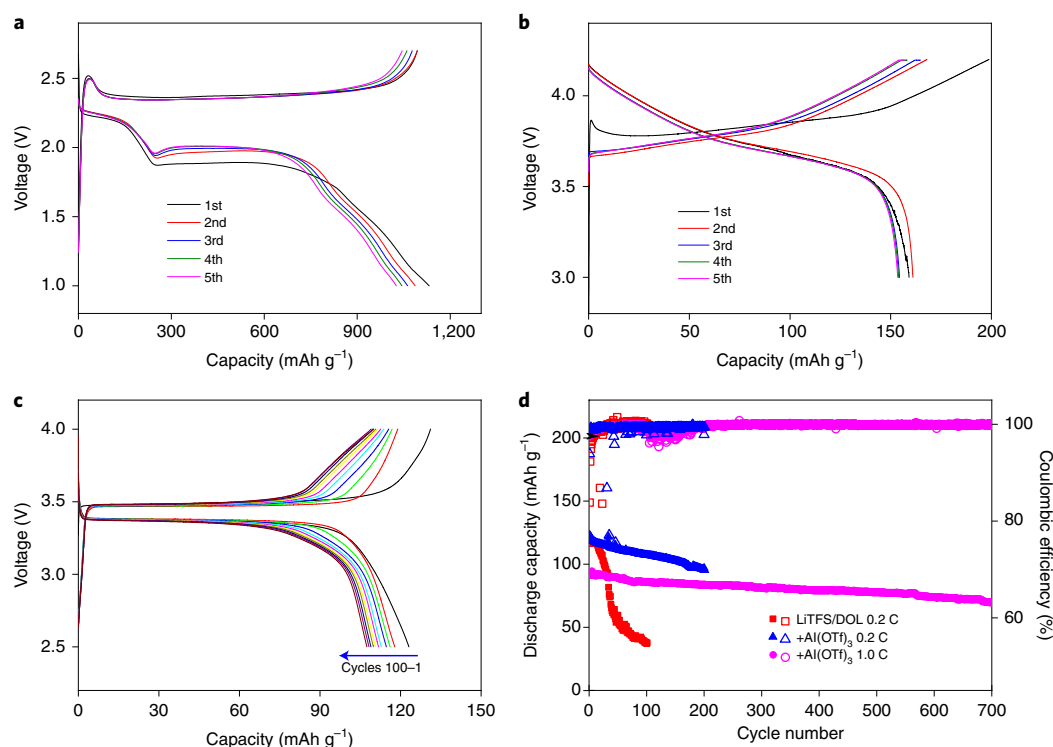


**Fig. 6 | Full cell demonstration of electrochemical cells using a Li metal anode and poly-DOL SPEs. a–c,** Discharge/charge profiles for Li/poly-DOL SPE/sulfur cells at 0.1C (a), Li/poly-DOL SPE/NCM (622) cells at 0.1C (b) and Li/poly-DOL SPE/LFP cells at 0.2C (c). The arrow in c indicates the slight fading of capacity from 1 to 100 cycles. **d,** Corresponding galvanostatic cycling performances and Coulombic efficiencies of Li//DOL//LFP (red) and Li/poly-DOL SPE/LFP cells (blue and purple).

This phenomenon is also confirmed by the high oxygen ratio on the surface according to the EDX spectra. In comparison, the major peaks of poly-DOL belong to the segment of polymer chain (Fig. 4l)<sup>45</sup>. Meanwhile, the liquid DOL electrolyte also undergoes more serious reduction of salts, and typical LiF peaks (Fig. 4f) and Li<sub>2</sub>S (Fig. 4g) peaks are detected<sup>29,45</sup>. Poly-DOL SPEs can also generate a considerable amount of LiF on their surfaces (Fig. 4j), which has now been well acknowledged in the literature as beneficial for stable Li deposition<sup>46</sup>. However, the less conductive Li<sub>2</sub>S is very small on the Li surface (Fig. 4k). Furthermore, we found that the aluminium species tends to slowly move to the interfaces between the Li anode and SPE. As shown for a cycled Li anode with poly-DOL SPE (Fig. 4l), a broad peak belong to the aluminium element is found on the surface of the Li anode. The aluminium complex (AlF<sub>3</sub> and Al<sub>2</sub>O<sub>3</sub>) is also crucial in stabilizing the Li electrode<sup>47,48</sup>. We conclude that during battery operation, polymerization of DOL also occurs by reduction of DOL at the surface of the Li anode. An advantage of the in situ-formed SPE is that the majority of the electrolyte solvent is polymerized, rather than just a relatively thin layer at the electrode surfaces.

The morphology of Li electrodeposits in liquid DOL electrolytes and in situ-formed poly-DOL SPEs can be probed directly using optical visualization studies. Because the measurements are performed without a separator, they allow us to eliminate any effects of separator pressure on the observations. For the symmetrical cells using liquid electrolyte, mossy Li electrodeposits are apparent as early as ten minutes after inception of the deposition (Fig. 5a). The uneven loose Li deposits are large enough to be seen clearly by the unaided eye (Fig. 5b). These observations are consistent with failure mechanisms already inferred from the analysis in Fig. 3, but they clearly provide a more critical/accelerated assessment of the shortcomings of the liquid DOL electrolyte. In comparison, Li plating

observed using poly-DOL SPEs is more compact. Indeed, when viewed either by optical (Fig. 5c) or scanning electron microscopy (SEM; Fig. 5d) methodologies even after 2 mAh cm<sup>-2</sup>, the surface of the electrodeposited Li remains visibly flat. We therefore propose that both the mechanical and chemical stability imparted by polymerizing the liquid DOL electrolytes lead to obvious improvements in the uniformity of Li plating. The elasticity of poly-DOL SPEs provides a mechanism for the interphase to flex and stretch, without cracking, to accommodate volume change during electrodeposition, which we believe facilitates uniform electrodeposition of Li. The polymerization of DOL to form SPEs is also thought to enhance the already good chemical stability of DOL in contact with metallic Li. In that case, the side reactions towards the metal surface are suppressed. This combination of features, including the organic elastic polymer, aluminium complex and LiF-rich inorganic compounds, is considered responsible for the impressive interfacial properties of SPEs.

### Full cell demonstration of in situ-formed SPEs

The advantages of in situ-formed SPEs make them suitable for rechargeable Li metal batteries using various cathode materials, such as sulfur, Li–LiNi<sub>0.6</sub>Mn<sub>0.2</sub>Co<sub>0.2</sub>O<sub>2</sub> (NMC) and LiFePO<sub>4</sub> (LFP). Li–S batteries have been widely studied for their high theoretical gravimetric energy density. The dissolution of lithium polysulfide in electrolytes and parasitic reactions with Li is a major problem. Although LiNO<sub>3</sub> is a good additive that can increase the stability of Li and is believed to work in tandem with lithium polysulfide to form a stable protective layer for high cell-level Coulombic efficiencies, LiNO<sub>3</sub> lowers the voltage stability window of Li–S batteries<sup>49</sup>. Here, we hypothesize that an SPE that does not use LiNO<sub>3</sub> as an additive would be effective in stabilizing the Li–S cell for a more fundamental reason—it would inhibit the dissolution of

polysulfide. As demonstrated in Fig. 6a, Li-S cells using the poly-DOL SPE electrolyte and a CMK-3 (an ordered mesoporous carbon material)/sulfur composite cathode can be operated under a wider voltage range and display high Coulombic efficiencies close to 100%, in comparison with the DOL electrolyte (Supplementary Figs. 13 and 14). Capacity–voltage curves for Li-S cells using the poly-DOL SPE also display two typical discharge peaks and one charging peak (Supplementary Fig. 15). The cycling performance is also noticeably improved relative to the liquid DOL electrolyte. The Coulombic efficiency remains over 98% after 100 cycles, even at a relatively small discharge/charge rate of 0.1 C (about  $0.3 \text{ mA cm}^{-2}$ ) (Supplementary Fig. 16). Notably, these benefits of the poly-DOL SPEs are also apparent at current densities as high as 0.5 C.

The success of the poly-SPE as an electrolyte for a conversion cathode is just one test of our hypothesis that underpins its impact. Additional tests include whether such electrolytes can function with intercalating cathodes, where, conventionally, electrolyte permeation into the porous cathode architecture is a requirement for good ion transport in the electrode. Here, we evaluate this possibility using cycling studies of Li/poly-DOL SPE/NMC (622) and Li/poly-DOL SPE/LFP cells. Fig. 6b shows the discharge/charge curves for solid-state Li/poly-DOL SPE/NMC (622) cells. Compared with the corresponding Li/DOL/NMC (622) cells, which exhibit low Coulombic efficiencies and fast capacity fading (Supplementary Fig. 17), the solid-state batteries display both high Coulombic efficiencies and excellent reversibility. The corresponding results for the solid-state Li/poly-DOL SPE/LFP batteries are reported in Fig. 6c. These cells are likewise observed to display high levels of reversibility and nearly flat discharge plateaus for over 100 charge–discharge cycles at room temperature (Fig. 6c and Supplementary Figs. 18 and 19). The results from higher-rate (1 C) and longer-term cycling studies reported in Fig. 6d show that Coulombic efficiencies close to 100%, and relatively stable cycling, are achieved even after 700 cycles. When an ex situ-formed SPE is used for Li-LFP cells, very large polarization is observed, even at low rates (Supplementary Fig. 20).

## Conclusions

We report that initiating polymerization of liquid electrolytes inside an electrochemical cell using low concentrations of soluble  $\text{Al}(\text{OTf})_3$  salt provides a powerful approach for creating SPEs with  $\text{mS cm}^{-1}$  levels of room temperature ionic conductivity and low interfacial impedances. As a result, the SPEs developed in this study do not suffer from limitations associated with poor bulk and interfacial ion transport common to all SSEs. Deployment of SPEs as electrolytes in symmetric Li/Li and asymmetric Li/Cu cells shows that they enable high cell-level Coulombic efficiency and excellent reversibility in Li stripping/plating processes. As a final demonstration, we use the electrolytes to create solid-state batteries utilizing conversion (for example, sulfur) and intercalating (for example, LFP and NMC) cathode chemistries. In so doing, we show that in situ polymer generation in an electrochemical cell provides a promising path to solid-state batteries in a range of chemistries.

## Methods

**Electrolyte preparation.** Electrolyte preparation and cell assembly were conducted in an argon gas-filled glove box (Inert), in which both the  $\text{O}_2$  and  $\text{H}_2\text{O}$  content were maintained below 0.5 ppm. The raw materials, including LiTFSI (TCI America;  $\geq 98.0\%$ ) and  $\text{Al}(\text{OTf})_3$  (Alfa Aesar; 99%), were stored in the glove box and used without further purification. Before all experiments, DOL (anhydrous; contains  $\sim 75$  ppm butylated hydroxytoluene as an inhibitor; 99.8%; Sigma–Aldrich) was treated overnight with coarse pieces of sacrificial metallic Li foil to chemically ‘dry’ the materials through reaction of the sacrificial Li with any traces of water remaining in the electrolytes. Liquid DOL–LiTFSI and DOL– $\text{Al}(\text{OTf})_3$  electrolytes containing different contents of the respective salts were prepared by adding the desired stoichiometric amounts of salt into DOL with vigorous stirring. Electrolyte compositions used in the study were created by diluting the homogeneous solutions of DOL– $\text{Al}(\text{OTf})_3$  with appropriate amounts of DOL–LiTFSI to create initially liquid DOL electrolytes containing variable fractions of  $\text{Al}(\text{OTf})_3$ .

**Cathode and battery preparation.** Sulfur cathodes were prepared by mixing sulfur/CMK-3 composites, Super P carbon as a conductivity aid, and polyvinylidene fluoride at a weight ratio of 84:8:8 in NMP solvent to form a smooth slurry. The slurry was ball milled for half an hour and painted on a carbon-coated aluminium foil. The cathodes were dried in a vacuum oven to remove the NMP solvent. The sulfur loading of each cathode was about  $2.0 \text{ mg cm}^{-2}$ . LFP cathodes were prepared by a similar procedure, and the LFP loading was about  $5 \text{ mg cm}^{-2}$ . CMK-3/sulfur composites were prepared using a typical melting–diffusion method<sup>30</sup>. The sulfur content was about 60 wt% in the CMK-3/sulfur composites. Nickel cobalt manganese oxide (NCM (622)) cathodes were obtained from Electrodes and More. Coin 2032-type cells were assembled using Li foil as the anode and glass fibre or Celgard 3501 as the separator. The separator was used in the assembly of cells to provide separation and control the thickness of the SPE, which can avoid short circuit in the liquid state. For prepared free-standing SPEs, no separator was used. All electrochemical cell performances were tested under room temperature.

**Material characterizations.** Liquid LiTFSI–DOL electrolytes and poly-DOL electrolytes were dissolved in dimethyl sulfoxide- $d_6$  for  $^1\text{H}$  NMR and  $^{13}\text{C}$  NMR analysis. GPC measurements were performed by first dissolving the synthesized poly-DOL electrolytes in THF and eluting the solutions in a Waters ambient temperature GPC equipped with triple detection capability for absolute polymer molecular weight determination. FTIR spectra of the materials were characterized using a Thermo Scientific spectrometer in the attenuated total reflection mode. d.c conductivity and electrochemical impedance spectroscopy were performed using a Novocontrol broadband dielectric/impedance spectrometer. The morphologies of Li after plating were imaged by field emission SEM. DSC was tested using a Q1000 Modulated Differential Scanning Calorimeter (TA Instruments). Oscillatory shear rheology was conducted using a strain-controlled ARES-LS (Rheometric Scientific) rheometer outfitted with cone and plate geometry (10 mm diameter;  $4^\circ$  cone angle) to monitor the polymerization reaction in real time. The oscillatory shear experiments were carried out with strain  $\gamma = 1\%$  and angular frequency  $\omega = 1 \text{ rad s}^{-1}$  at ambient temperature ( $24^\circ\text{C}$ ) for 2 h. Reaction components were taken out of the glove box and mixed before they were loaded in the instrument. For small-amplitude oscillatory shear measurements, frequency sweeps from 0.1 to  $100 \text{ rad s}^{-1}$  were performed at a shear strain  $\gamma = 0.1\%$  to study the response of materials in the linear viscoelastic regime. Tensile measurements were performed at ambient temperature using a stress-controlled DMA Q800 (TA Instruments). Materials were taken directly from the glove box before they were loaded. TGA tests were performed at room temperature to  $500^\circ\text{C}$  under an  $\text{N}_2$  atmosphere at a temperature increase of  $5^\circ\text{C min}^{-1}$ . The instrument used for TGA testing was a TG/DTA 6200. Raman tests were conducted using a Renishaw inVia confocal Raman microscope at an excitation wavelength of 785 nm. AnSSX-100 XPS spectrometer was used to study SEI layers on the Li surface. The cycled Li was washed sufficiently with DOL and dimethoxyethane and dried in the glove box.

**Electrochemical cells test.** The in situ Li plating images were recorded using a Dino-Lite digital microscope. A homemade cuvette cell with two parallel Li electrodes inside was used to observe morphological changes of Li surfaces in real time. Galvanostatic discharge/charge tests were performed using a Neware battery tester at room temperature. A CH 600E electrochemical workstation was used for the cyclic voltammetry measurements. The electrochemical floating experiments were conducted in Li||NMC cells, which were charged to 4.2 V first, then held at progressively higher voltages, each for a period of 10 h.

## Data availability

The data that support the plots within this paper and other findings of this study are available from the corresponding author upon reasonable request.

Received: 18 September 2018; Accepted: 8 February 2019;

Published online: 11 March 2019

## References

- Armand, M. & Tarascon, J. M. Building better batteries. *Nature* **451**, 652–657 (2008).
- Whittingham, M. S. Ultimate limits to intercalation reactions for lithium batteries. *Chem. Rev.* **114**, 11414–11443 (2014).
- Choi, J. W. & Aurbach, D. Promise and reality of post-lithium-ion batteries with high energy densities. *Nat. Rev. Mater.* **1**, 16013 (2016).
- Tikekar, M. D., Choudhury, S., Tu, Z. & Archer, L. A. Design principles for electrolytes and interfaces for stable lithium-metal batteries. *Nat. Energy* **1**, 16114 (2016).
- Cheng, X. B., Zhang, R., Zhao, C. Z. & Zhang, Q. Toward safe lithium metal anode in rechargeable batteries: a review. *Chem. Rev.* **117**, 10403–10473 (2017).
- Lin, D., Liu, Y. & Cui, Y. Reviving the lithium metal anode for high-energy batteries. *Nat. Nanotechnol.* **12**, 194–206 (2017).
- Bai, P., Li, J., Brushett, F. R. & Bazant, M. Z. Transition of lithium growth mechanisms in liquid electrolytes. *Energy Environ. Sci.* **9**, 3221–3229 (2016).



8. Busche, M. R. et al. Dynamic formation of a solid–liquid electrolyte interphase and its consequences for hybrid-battery concepts. *Nat. Chem.* **8**, 426–434 (2016).
9. Wei, S., Choudhury, S., Tu, Z., Zhang, K. & Archer, L. A. Electrochemical interphases for high-energy storage using reactive metal anodes. *Acc. Chem. Res.* **51**, 80–88 (2018).
10. Liu, K., Liu, Y., Lin, D., Pei, A. & Cui, Y. Materials for lithium-ion battery safety. *Sci. Adv.* **4**, eaas9820 (2018).
11. Li, G. et al. Self-formed hybrid interphase layer on lithium metal for high-performance lithium–sulfur batteries. *ACS Nano* **12**, 1500–1507 (2018).
12. Li, N.-W., Yin, Y.-X., Yang, C.-P. & Guo, Y.-G. An artificial solid electrolyte interphase layer for stable lithium metal anodes. *Adv. Mater.* **28**, 1853–1858 (2016).
13. Qian, J. et al. High rate and stable cycling of lithium metal anode. *Nat. Commun.* **6**, 6362 (2015).
14. Suo, L. M. et al. “Water-in-salt” electrolyte enables high-voltage aqueous lithium-ion chemistries. *Science* **350**, 938–943 (2015).
15. Zeng, Z. et al. Non-flammable electrolytes with high salt-to-solvent ratios for Li-ion and Li-metal batteries. *Nat. Energy* **3**, 674–681 (2018).
16. Tu, Z. et al. Nanoporous hybrid electrolytes for high-energy batteries based on reactive metal anodes. *Adv. Energy Mater.* **7**, 1602367 (2017).
17. Zhou, W. et al. Plating a dendrite-free lithium anode with a polymer/ceramic/polymer sandwich electrolyte. *J. Am. Chem. Soc.* **138**, 9385–9388 (2016).
18. Manthiram, A., Yu, X. W. & Wang, S. F. Lithium battery chemistries enabled by solid-state electrolytes. *Nat. Rev. Mater.* **2**, 16103 (2017).
19. Gao, Z. et al. Promises, challenges, and recent progress of inorganic solid-state electrolytes for all-solid-state lithium batteries. *Adv. Mater.* **30**, e1705702 (2018).
20. Hood, Z. D., Wang, H., Samuthira Pandian, A., Keum, J. K. & Liang, C. Li<sub>2</sub>O/Cl crystalline electrolyte for stable metallic lithium anodes. *J. Am. Chem. Soc.* **138**, 1768–1771 (2016).
21. Quartarone, E. & Mustarelli, P. Electrolytes for solid-state lithium rechargeable batteries: recent advances and perspectives. *Chem. Soc. Rev.* **40**, 2525–2540 (2011).
22. Zhu, Z. et al. All-solid-state lithium organic battery with composite polymer electrolyte and pillar[5]quinone cathode. *J. Am. Chem. Soc.* **136**, 16461–16464 (2014).
23. Manuel Stephan, A. Review on gel polymer electrolytes for lithium batteries. *Eur. Polym. J.* **42**, 21–42 (2006).
24. Lu, Q. et al. Dendrite-free, high-rate, long-life lithium metal batteries with a 3D cross-linked network polymer electrolyte. *Adv. Mater.* **29**, 1604460 (2017).
25. Bae, J. et al. A 3D nanostructured hydrogel-framework-derived high-performance composite polymer lithium-ion electrolyte. *Angew. Chem. Int. Ed.* **57**, 2096–2100 (2018).
26. Dong, T. et al. A multifunctional polymer electrolyte enables high-voltage lithium metal battery ultra-long cycle-life. *Energy Environ. Sci.* **11**, 1197–1203 (2018).
27. Sun, B. et al. Toward solid-state 3D-microbatteries using functionalized polycarbonate-based polymer electrolytes. *ACS Appl. Mater. Interfaces* **10**, 2407–2413 (2018).
28. Lin, Y., Wang, X., Liu, J. & Miller, J. D. Natural halloysite nano-clay electrolyte for advanced all-solid-state lithium-sulfur batteries. *Nano Energy* **31**, 478–485 (2017).
29. Pan, Q. et al. Correlating electrode–electrolyte interface and battery performance in hybrid solid polymer electrolyte-based lithium metal batteries. *Adv. Energy Mater.* **7**, 1701231 (2017).
30. Mindemark, J., Imholt, L., Montero, J. & Brandell, D. Allyl ethers as combined plasticizing and crosslinkable side groups in polycarbonate-based polymer electrolytes for solid-state Li batteries. *J. Polymer Sci. A* **54**, 2128–2135 (2016).
31. Nair, J. R. et al. Truly quasi-solid-state lithium cells utilizing carbonate free polymer electrolytes on engineered LiFePO<sub>4</sub>. *Electrochim. Acta* **199**, 172–179 (2016).
32. Li, S. et al. A superionic conductive, electrochemically stable dual-salt polymer electrolyte. *Joule* **2**, 1838–1856 (2018).
33. Ma, Q. et al. Single lithium-ion conducting polymer electrolytes based on a super-delocalized polyanion. *Angew. Chem. Int. Ed.* **55**, 2521–2525 (2016).
34. Porcarelli, L. et al. Single ion conducting polymer electrolytes based on versatile polyurethanes. *Electrochim. Acta* **241**, 526–534 (2017).
35. Nykaza, J. R. et al. Polymerized ionic liquid diblock copolymer as solid-state electrolyte and separator in lithium-ion battery. *Polymer* **101**, 311–318 (2016).
36. Pelz, A. et al. Self-assembled block copolymer electrolytes: enabling superior ambient cationic conductivity and electrochemical stability. *Chem. Mater.* **31**, 277–285 (2018).
37. Raccichini, R., Dibden, J. W., Brew, A., Owen, J. R. & Garcia-Araez, N. Ion speciation and transport properties of LiTFSI in 1,3-dioxolane solutions: a case study for Li–S battery applications. *J. Phys. Chem. B* **122**, 267–274 (2018).
38. Okada, M., Yamashita, Y. & Ishii, Y. Polymerization of 1,2-dioxolane. *Makromolekul. Chem.* **80**, 196–207 (1964).
39. Hiemenz, P. C. & Lodge, T. P. *Polymer Chemistry* 2nd edn 447–448 (CRC Press, 2007).
40. Erk, K. A., Martin, J. D., Hu, Y. T. & Shull, K. R. Extreme strain localization and sliding friction in physically associating polymer gels. *Langmuir* **28**, 4472–4478 (2012).
41. He, M. et al. Fluorinated electrolytes for 5-V Li-ion chemistry: probing voltage stability of electrolytes with electrochemical floating test. *J. Electrochem. Soc.* **162**, A1725–A1729 (2015).
42. Wood, K. N. et al. Dendrites and pits: untangling the complex behavior of lithium metal anodes through operando video microscopy. *ACS Central Sci.* **2**, 790–801 (2016).
43. Aurbach, D. et al. On the surface chemical aspects of very high energy density, rechargeable Li–sulfur batteries. *J. Electrochem. Soc.* **156**, A694–A702 (2009).
44. Verma, P., Maire, P. & Novák, P. A review of the features and analyses of the solid electrolyte interphase in Li-ion batteries. *Electrochim. Acta* **55**, 6332–6341 (2010).
45. Wang, Y. et al. Electrochemically controlled solid electrolyte interphase layers enable superior Li–S batteries. *ACS Appl. Mater. Interfaces* **10**, 24554–24563 (2018).
46. Lu, Y., Tu, Z. & Archer, L. A. Stable lithium electrodeposition in liquid and nanoporous solid electrolytes. *Nat. Mater.* **13**, 961–969 (2014).
47. Wang, H., Lin, D., Liu, Y., Li, Y. & Cui, Y. Ultrahigh-current density anodes with interconnected Li metal reservoir through overlithiation of mesoporous AlF<sub>3</sub> framework. *Sci. Adv.* **3**, e1701301 (2017).
48. Tu, Z. Y. et al. Stabilizing protic and aprotic liquid electrolytes at high-bandgap oxide interphases. *Chem. Mater.* **30**, 5655–5662 (2018).
49. Zhang, S. S. Effect of discharge cutoff voltage on reversibility of lithium/sulfur batteries with LiNO<sub>3</sub>-contained electrolyte. *J. Electrochem. Soc.* **159**, A920–A923 (2012).
50. Ji, X., Lee, K. T. & Nazar, L. F. A highly ordered nanostructured carbon–sulfur cathode for lithium–sulfur batteries. *Nat. Mater.* **8**, 500–506 (2009).

## Acknowledgements

This work was supported by the Department of Energy Basic Energy Sciences programme through award DE-SC0016082. Electron microscopy and XPS analysis were performed in facilities supported by the Cornell Center for Materials Research with funding from the NSF MRSEC programme (DMR-1719875). Q.Z. thanks B. Abel and H. Johnson from the Coates Research Group for fruitful discussions about DOL polymerization.

## Author contributions

Q.Z. and L.A.A. conceived and designed the experiments. Q.Z. prepared and characterized the polymer electrolyte, as well as electrochemical performance. X.L. and Q.Z. performed thermal and rheology studies of SPEs. Q.Z., X.L. and L.A.A. wrote the original draft. Q.Z. and L.A.A. further wrote and revised the manuscript. All authors contributed to the data analysis. L.A.A. directed the research.

## Competing interests

The authors declare no competing interests.

## Additional information

**Supplementary information** is available for this paper at <https://doi.org/10.1038/s41560-019-0349-7>.

**Reprints and permissions information** is available at [www.nature.com/reprints](http://www.nature.com/reprints).

**Correspondence and requests for materials** should be addressed to L.A.A.

**Publisher's note:** Springer Nature remains neutral with regard to jurisdictional claims in published maps and institutional affiliations.

© The Author(s), under exclusive licence to Springer Nature Limited 2019